MODELLING OF LAMB WAVES IN COMPOSITE LAMINATED PLATES EXCITED BY INTERDIGITAL TRANSDUCERS

M. Veidt *
Department of Mechanical Engineering
The University of Queensland
Brisbane, Qld 4072, Australia

T. Liu
Department of Civil Engineering
The University of Queensland
Brisbane, Qld 4072, Australia

S. Kitipornchai
Department of Building and Construction
City University of Hong Kong, Kowloon, Hong Kong

* corresponding author:

phone: +61 7 3365 3621
fax: +61 7 3365 4799
email: m.veidt@uq.edu.au

ABSTRACT

The technique of permanently attaching interdigital transducers (IDT) to either flat or curved structural surfaces to excite single Lamb wave mode has demonstrated great potential for quantitative non-destructive evaluation and smart materials design. In this paper, the acoustic wave field in a composite laminated plate excited by an IDT is investigated. Based on the discrete layer theory and a multiple integral transform method, an analytical-numerical approach is developed to evaluate the surface velocity response of the plate due to the IDT's excitation. In this approach, the frequency spectrum and wave number spectrum of the output of IDT are obtained directly. The corresponding time domain results are calculated by applying a standard inverse fast Fourier transformation technique. Numerical examples are presented to validate the developed method and show the ability of mode selection and isolation. A new effective way of transfer function estimation and interpretation is presented by considering the input wave number spectrum in addition to the commonly used input frequency spectrum. The new approach enables the simple physical evaluation of the influences of IDT geometrical features such as electrode finger widths and overall dimension and excitation signal properties on the input-output characteristics of IDT. Finally, considering the convenience of Mindlin plate wave theory in numerical computations as well as theoretical analysis, the validity is examined of using this approximate theory to design IDT for the excitation of the first and second anti-symmetric Lamb modes.

1 INTRODUCTION

It has been well recognized that guided Lamb wave techniques can provide a very sensitive and effective means for structural condition monitoring and smart materials design, [1]. However, since in these techniques multiple wave modes are generally generated and the individual modes are usually dispersive, the received signals are very complex and difficult to interpret. An attractive way to deal with this problem has recently been introduced by applying interdigital transducer (IDT) technologies, which are commonly used in electronic systems, [2]. The basic configuration of an IDT consists of an interdigital electrode pattern deposited on a piezoelectric substrate. Through careful design of the electrode pattern and the application of an excitation pulse with a specified frequency content, a particular single wave mode can be generated in the substrate. This offers the possibility to limit the wave length as well as the frequency bandwith of the excited waves. Hence, the number of excited wave modes as well as the dispersion characteristics can be controlled. This concept has attracted much attention in the structural health monitoring and smart materials design community in recent years, e.g. [3,4].

To enable the design of optimised IDT for a specific application, the possibility to accurately model its transfer characteristics is essential. Recently some pioneering work has been done by Cawley and his co-workers [5]. Initially, they used time marching finite element techniques to model the acoustic Lamb wave fields excited by IDT. It was shown that this method is extremely time-consuming and hence not suitable as a design tool. Therefore, they investigated an alternative approach based on Huygens' principle. Using this approach, the acoustic field excited by straight and curved finger IDT attached to isotropic plates has been successfully modelled. However, for IDT attached to composite laminated plates, the point source solution, which is required as the fundamental building block in the Huygen's principle method, is very complex, and the approach seems not to be convenient for evaluation and interpretation of the corresponding results.

In view of this, this paper presents a new approach based on a combination of a multiple integral transform method and a discrete layer theory to model the acoustic wave field excited by IDT attached to an orthotropic composite laminated plate. Unlike the existing

methods, this approach does not require to divide the IDT finger area into elements, but treats it exactly. In addition, the frequency as well as the wave number spectrum are directly calculated, which are essential tools for the interpretation of the excited wave field.

2 FORMULATION OF THE PROBLEM

The problem considered is shown in Fig. 1. An IDT driven by an arbitrary function generator is attached to the surface of a composite laminated plate. The excited Lamb wave is sensed some distance away from the transmitter using a non-contact sensor, for example a laser vibrometer measuring the out-of-plane surface velocity component of the travelling wave at the measurement location. The purpose of this study is to theoretically evaluate the input-output transfer characteristics of the measurement system.

For simplicity only the two-dimensional plain strain case is considered. The composite laminated plate is confined to cross-ply laminates, and the fingers of the IDT are aligned with one of the principal material directions of the laminate.

In order to model the wave propagation behaviour, the so-called stiffness method or discrete layer theory is used, e.g. [6,8]. The main idea of this method is to divide the plate into a number of mathematical layers in the thickness direction and to approximate the through thickness displacement variation within each layer by interpolation polynomials. Using the principle of virtual work, the differential equation of the wave motion in the plate can then be expressed as a function of the in-plane coordinates alone.

Following the procedures described in [6-8] the governing equation for the *i*th layer can be expressed as

$$\mathbf{M}^{(i)} \frac{\partial^2}{\partial t^2} \mathbf{q}_i + \left[-\mathbf{K}_1^{(i)} \frac{\partial^2}{\partial x^2} - \mathbf{K}_4^{(i)} \frac{\partial}{\partial x} + \mathbf{K}_6^{(i)}\right] \mathbf{q}_i = \mathbf{T}_i \qquad (1)$$

where t is the time variable, x is a principal material direction, $\mathbf{q}_i$ is the specific displacement vector comprised of the displacement vectors at the upper surface, the middle plane and the lower surface of the layer, $\mathbf{T}_i$ is the external load vector, and $\mathbf{M}^{(i)}$, $\mathbf{K}_1^{(i)}$, $\mathbf{K}_4^{(i)}$ and $\mathbf{K}_6^{(i)}$ are 6×6 system matrices, which are given in Appendix A1. In the derivation of (1) it is assumed that no body force is acting.

Assembling the governing equations for the n layers from top to bottom yields the governing equation of the laminated plate

$$\mathbf{M}\frac{\partial^2}{\partial t^2}\mathbf{q} + [-\mathbf{K}_1\frac{\partial^2}{\partial x^2} - \mathbf{K}_4\frac{\partial}{\partial x} + \mathbf{K}_6]\,\mathbf{q} = \mathbf{T} \tag{2}$$

where $\mathbf{q}$, $\mathbf{T}$, $\mathbf{M}$, $\mathbf{K}_1$, $\mathbf{K}_4$, and $\mathbf{K}_6$ are the global vectors and matrices produced by the summation of $\mathbf{q}_i$, $\mathbf{T}_i$, $\mathbf{M}^{(i)}$, $\mathbf{K}_1^{(i)}$, $\mathbf{K}_4^{(i)}$ and $\mathbf{K}_6^{(i)}$ (i=1,2,3, … n), respectively.

Following [5], it is assumed that: (1) the IDT generates primarily normal pressure on the surface of the plate, (2) the normal pressure produced by every finger element is considered as a piston or a parabolic distribution source. With these assumptions and the geometry parameters introduced in Fig. 2 the pressure $p_k(x,t)$ produced on the surface of the plate by the kth finger of the IDT is expressed as

$$p_k(x,t) = p_0(t)D_k(x), \quad (k-1)d - a_k \le x \le (k-1)d + a_k, \quad k=1,2,\ldots n_f \tag{3}$$

where $p_0(t)$ is a known function of time t, a_k is half the width of the kth finger, d is the distance between the centers of two adjacent fingers, n_f is the number of fingers, and $D_k(x)$ is the pressure distribution function, which for a piston distribution is defined by

$$D_k(x) = (-1)^k \tag{4a}$$

and for parabolic distribution is defined by

$$D_k(x) = (-1)^k \frac{3}{2}\left\{1 - \left[\frac{x-(k-1)d}{a_k}\right]^2\right\}. \tag{4b}$$

where the 180° phase difference between two adjacent fingers has been taken into account and the resultant excitation force is equal in both cases.

With (3) and (4) the global load vector in (2) is

$$\mathbf{T} = p_0(t)\sum_{k=1}^{n_f}\{D_k(x)[H(x-x_k+a_k) - H(x-x_k-a_k)]\}\,\mathbf{C} \tag{5}$$

where $x_k = (k-1)d$, and $\mathbf{C}$ is a constant vector of length $2(2n+1)$, which is given as

$$\mathbf{C}^{\mathrm{T}} = [0,1,0,0,0,\ldots,0,0]. \tag{6}$$

3 DISCRETE LAYER THEORY SOLUTION

In order to solve the system equations, the following Fourier time and spatial transforms are introduced

$$\bar{g}(x,\omega) = \int_0^{\infty} g(x,t)e^{-i\omega t}\,dt \tag{7a}$$

$$\tilde{g}(\kappa,t) = \int_{-\infty}^{+\infty} g(x,t)e^{-i\kappa x}\,dx\,. \tag{7b}$$

Applying these transformations to (2) yields

$$(\kappa^2\mathbf{K}_1 - i\kappa\mathbf{K}_4 + \mathbf{K}_6 - \omega^2\mathbf{M})\,\tilde{\bar{\mathbf{q}}} = \tilde{\bar{\mathbf{T}}} \tag{8}$$

For a given ω, (8) describes a quadratic eigenvalue equation in κ, which can be written as

$$(\mathbf{Q} - \lambda\mathbf{R})\varphi = \mathbf{f} \tag{9}$$

where

$$\mathbf{Q} = \begin{bmatrix} \mathbf{0} & \mathbf{I} \\ \omega^2\mathbf{M} - \mathbf{K}_6 & -\mathbf{K}_4 \end{bmatrix}, \qquad \mathbf{R} = \begin{bmatrix} \mathbf{I} & \mathbf{0} \\ \mathbf{0} & -\mathbf{K}_1 \end{bmatrix}, \tag{10a,b}$$

$$\varphi^{\mathrm{T}} = [\,\tilde{\bar{\mathbf{q}}}^{\mathrm{T}} \quad \lambda\,\tilde{\bar{\mathbf{q}}}^{\mathrm{T}}\,], \qquad \mathbf{f}^{\mathrm{T}} = [\mathbf{0} \quad -\tilde{\bar{\mathbf{T}}}^{\mathrm{T}}], \qquad \lambda = -i\kappa \tag{10c-e}$$

I and **0** are identity and zero matrices, respectively, which have the same dimension as the system matrices **M**, $\mathbf{K}_1$, $\mathbf{K}_4$, and $\mathbf{K}_6$.

Using the mode summation method introduced for example in [9], the solution of (9) can be expressed as

$$\varphi = \sum_{\mathrm{m}=1}^{2\mathrm{M}} \frac{\psi_{\mathrm{m}}^{T}\mathbf{f}\varphi_{\mathrm{m}}}{(\lambda - \lambda_{\mathrm{m}})\psi_{\mathrm{m}}^{T}\mathbf{R}\varphi_{\mathrm{m}}} \tag{11}$$

where $M=2(2n+1)$, φ_{m} are the eigenvectors of the homogenous form of equation (9), ψ_{m} are the eigenvectors of the accompanying equation of (9), which is

$$(\mathbf{Q}^{\mathrm{T}} - \lambda\mathbf{R}^{\mathrm{T}})\psi = \mathbf{0} \tag{12}$$

and λ_{m} are the corresponding eigenvalues.

Substituting (10c) and (10e) into (11) yields the solution of (8)

$$\tilde{\bar{\mathbf{q}}} = i\sum_{m=1}^{2M} \frac{\boldsymbol{\phi}_{ml}^{\mathrm{T}}\,\tilde{\bar{\mathbf{T}}}}{(\kappa - \kappa_m)\boldsymbol{\phi}_m^{\mathrm{T}}\mathbf{R}\boldsymbol{\psi}_m}\boldsymbol{\psi}_{mu} \tag{13}$$

where $\boldsymbol{\psi}_{mu}$, $\boldsymbol{\phi}_{ml}$ are the upper and lower halves of the eigenvectors $\boldsymbol{\psi}_m$ and $\boldsymbol{\phi}_m$, respectively.

Applying the integral transforms (7) to (5) yields

$$\tilde{\tilde{\mathbf{T}}} = \left[\overline{p}_0(\omega) \sum_{k=1}^{n_f} \int_{x_k - a_k}^{x_k + a_k} D_k(x) e^{-i\kappa x} dx \right] \mathbf{C} \tag{14}$$

Substituting (14) into (13) and applying the inverse Fourier spatial transform corresponding to (7b), results in the frequency domain solution of the displacement vector $\overline{\mathbf{q}}$

$$\overline{\mathbf{q}} = \frac{i}{2\pi} \overline{p}_0(\omega) \int_{-\infty}^{\infty} \sum_{m=1}^{2M} \frac{I_f(\kappa, x, \omega) \boldsymbol{\phi}_{ml}^T \mathbf{C}}{(\kappa - \kappa_m) \boldsymbol{\phi}_m^T \mathbf{R} \boldsymbol{\psi}_m} \boldsymbol{\psi}_{mu} d\kappa \tag{15}$$

where $I_f(\kappa, x, \omega)$ is for piston pressure distribution

$$I_f(\kappa, x, \omega) = \overline{p}_0(\omega) \sum_{k=1}^{n_f} (-1)^k \frac{i}{\kappa} \left\{ e^{i\kappa[x-(k-1)d-a_k]} - e^{i\kappa[x-(k-1)d+a_k]} \right\} \tag{16a}$$

or for parabolic pressure distribution

$$I_f(\kappa, x, \omega) = \overline{p}_0(\omega) \sum_{k=1}^{n_f} (-1)^k \frac{2}{a_k^2 \kappa^3} \left\{ (i - a_k\kappa) e^{i\kappa[x-(k-1)d-a_k]} - (i + a_k\kappa) e^{i\kappa[x-(k-1)d+a_k]} \right\} \tag{16b}$$

Using contour integration technique to evaluate (15), the frequency domain solution of the displacement field excited by the IDT is finally obtained as

$$\overline{\mathbf{q}} = -\overline{p}_0(\omega) \sum_{m=1}^{M_r + M_c} \frac{\boldsymbol{\phi}_{ml}^T \mathbf{C} \boldsymbol{\psi}_{mu}}{\boldsymbol{\phi}_m^T \mathbf{R} \boldsymbol{\psi}_m} I_f(\kappa, x, \omega) d\kappa \tag{17}$$

where M_r is the number of the real wave modes carrying energy towards the positive x axis direction, and M_c is the number of complex wave modes corresponding to the κ_m with $\mathrm{Im}(\kappa_m)>0$.

Considering the specific measurement system described above, the frequency domain solution of the out-of-plane velocity at the upper surface is

$$\overline{v}(x, \omega) = -i\omega \overline{p}_0(\omega) \sum_{m=1}^{M_r + M_c} \frac{(\boldsymbol{\phi}_{ml}^T \mathbf{C})(\boldsymbol{\psi}_{mu}^T \mathbf{C})}{\boldsymbol{\phi}_m^T \mathbf{R} \boldsymbol{\psi}_m} I_f(\kappa, x, \omega) \tag{18}$$

In this input-output transfer equation $\overline{p}_0(\omega)$ reflects the influence of the frequency content of the input signal, while $I_f(\kappa, x, \omega)$ describes the influence of the wave number characteristics of the IDT. It is shown below that these two terms produce two different

types of characteristic curves, which enable easy interpretation of the system's output and efficient design of optimised IDT.

Having obtained the frequency domain solution (18) the time domain solution is evaluated applying the inverse Fourier time transformation

$$v(x,t) = \frac{1}{2\pi}\int_{-\infty}^{\infty} \bar{v}(x,\omega) e^{i\omega t} d\omega \tag{19}$$

The computation of (19) is carried out using a conventional fast Fourier transformation (FFT) algorithm.

4 MINDLIN PLATE THEORY SOLUTION

In order to validate the discrete layer theory solutions, a closed form solution is derived in this section, which is based on the Mindlin plate theory for composite plates according to [10].

Using the coordinate system described in Fig. 2, the equations of motion for the plate in a state of plane strain parallel to the *x*-*z* plane are

$$k_s A_{55}\left(\frac{\partial \varphi_x}{\partial x} + \frac{\partial^2 w}{\partial x^2}\right) + p(x,t) = \rho h \frac{\partial^2 w}{\partial t^2} \tag{20a}$$

$$D_{11}\frac{\partial^2 \varphi_x}{\partial x^2} - k_s A_{55}(\varphi_x + \frac{\partial w}{\partial x}) = \frac{\rho h^3}{12}\frac{\partial^2 \varphi_x}{\partial t^2} \tag{20b}$$

where the external pressure is

$$p(x,t) = p_0(t)\sum_{k=1}^{n_f}\{D_k(x)[H(x-x_k+a_k) - H(x-x_k-a_k)]\} \tag{21}$$

In (20) w is the transverse displacement, φ_x is the rotation of a plane section around the y-axis, $k_s(=\pi^2/12)$ is the shear correction factor, and A_{55} and D_{11} are the plate's transverse-shear and bending rigidities, respectively, which are given as

$$A_{55} = \sum_{k=1}^{n} \overline{Q}_{55}^{(k)}(\bar{z}_{k+1} - \bar{z}_k), \quad D_{11} = \frac{1}{3}\sum_{k=1}^{n} \overline{Q}_{11}^{(k)}(\bar{z}_{k+1}^3 - \bar{z}_k^3) \tag{22a,b}$$

with

$$\overline{Q}_{55}^{(k)} = Q_{55}^{(k)}\cos^2\theta_k + Q_{44}^{(k)}\sin^2\theta_k, \quad \overline{Q}_{11}^{(k)} = Q_{11}^{(k)}\cos^4\theta_k + Q_{22}^{(k)}\sin^4\theta_k \tag{23a,b}$$

$$Q_{11}^{(k)} = E_1^{(k)}/(1-\nu_{12}^{(k)}\nu_{21}^{(\kappa)}), \quad Q_{22}^{(k)} = \nu_{12}^{(k)}E_2^{(k)}/(1-\nu_{12}^{(k)}\nu_{21}^{(\kappa)}) \tag{23c,d}$$

$$Q_{44}^{(k)} = G_{23}^{(k)}, \quad Q_{55}^{(k)} = G_{13}^{(k)}, \quad \nu_{21}^{(k)} = \nu_{12}^{(k)} E_2^{(k)} / E_1^{(k)} \tag{23e-g}$$

where $\bar{z}_k = z_k - h/2$, $c_{ii}^{(k)}$ (i=1,2,4,5) are the material stiffness constant of the kth layer, θ_k is the angle between the principal material direction of the kth layer and the x-axis (0° or 90°), and $E_1^{(k)}$, $E_2^{(k)}$, $G_{13}^{(k)}$, $G_{23}^{(k)}$ and $\nu_{12}^{(k)}$ are the engineering constants for the kth layer.

Using a similar Fourier transformation procedure as above, the frequency domain solution of the transverse surface velocity of the composite plate excited by the IDT is obtained as

for piston pressure distribution

$$\bar{v}(x,\omega) = i\omega \bar{p}_0(\omega) \sum_{k=1}^{n_f} (-1)^k \left\{ \mu_1 [e^{-i\kappa_1 (x - x_k - a_k)} - e^{-i\kappa_1 (x - x_k + a_k)}] + \mu_2 [e^{-\gamma (x - x_k - a_k)} - e^{-\gamma (x - x_k + a_k)}] \right\}, \quad \text{for } |\omega| \le \omega_c \tag{24a}$$

$$\bar{v}(x,\omega) = i\omega \bar{p}_0(\omega) \sum_{k=1}^{n_f} (-1)^k \left\{ \mu_1 [e^{-i\kappa_1 (x - x_k - a_k)} - e^{-i\kappa_1 (x - x_k + a_k)}] + \mu_2 [e^{-i\kappa_2 (x - x_k - a_k)} - e^{-i\kappa_2 (x - x_k + a_k)}] \right\}, \quad \text{for } |\omega| > \omega_c \tag{24b}$$

for parabolic pressure distribution

$$\bar{v}(x,\omega) = i\omega \bar{p}_0(\omega) \sum_{k=1}^{n_f} (-1)^k \left[\mu_{11} e^{-i\kappa_1 (x - x_k - a_k)} + \mu_{12} e^{-i\kappa_1 (x - x_k + a_k)} + \mu_{21} e^{-\gamma (x - x_k - a_k)} + \mu_{22} e^{-\gamma (x - x_k + a_k)} \right], \quad \text{for } |\omega| \le \omega_c \tag{25a}$$

$$\bar{v}(x,\omega) = i\omega \bar{p}_0(\omega) \sum_{k=1}^{n_f} (-1)^k \left[\mu_{11} e^{-i\kappa_1 (x - x_k - a_k)} + \mu_{12} e^{-i\kappa_1 (x - x_k + a_k)} + \mu_{21} e^{-i\kappa_2 (x - x_k - a_k)} + \mu_{22} e^{-i\kappa_2 (x - x_k + a_k)} \right], \quad \text{for } |\omega| > \omega_c \tag{25b}$$

where the cutoff frequency is $\omega_c = \sqrt{12 A_{55} k_s / (\rho h^3)}$. The coefficients μ_i and μ_{ij} (i,j=1,2) and the wave numbers κ_1, κ_2 and γ are given in Appendix A2.

5 NUMERICAL RESULTS AND DISCUSSION

First, some numerical results are presented illustrating the mode selection capability of IDT using the new discrete layer multiple integral transform methodology developed

above. Based on these results, the influence of various IDT design parameters on the excited wave field such as number of electrode fingers and finger apodisation are discussed. In addition, the discrete layer theory results are compared with predictions based on Mindlin plate theory, and the potential is investigated to use the simplified Mindlin plate theory model to predict the first and second anti-symmetric wave modes excited by IDT.

Two plates are used in the simulations: a) an isotropic aluminum plate (Al) and b) a graphite-epoxy fibre-reinforced composite laminated plate (G-E). The material properties of the isotropic plate and of the G-E lamina are given in Table 1.

The excitation signal is a Hanning windowed delayed sine pulse, which can be expressed as

$$p_0(t) = \begin{cases} 0.5[1-\cos(2\pi f_0 t / n_0)]\cos(2\pi f_0 t), & t \le n_0 / f_0 \\ 0, & t > n_0 / f_0 \end{cases} \tag{26}$$

where f_0 is the central frequency and n_0 is the number of sinusoidal cycles within the pulse.

Figs. 3 and 4 show the wave number-frequency and group velocity-frequency curves of a 2-mm thick aluminum plate and a (0°/90°/0°/90°/0°) graphite-epoxy laminate of the same thickness, which have been calculated by solving the eigenvalue equation (12). As indicated, they are used as graphical tools to illustrate the wave number and group velocity content of individual wave modes for an excitation signal with a certain frequency content.

Fig. 5 shows a comparison of the discrete layer multiple integral transformation simulation tool with the result based on Mindlin plate theory. The surface velocity time histories are displayed 300mm away from a 20 finger IDT, which is excited by a 15 cycles, 250kHz centre frequency input signal. The finger width is 0.5mm and the finger spacing is 3.77mm, which corresponds to a centre wave number of 833m^{-1}. Hence, according to Fig. 3, the target wave mode is the first anti-symmetric mode a_0. The two results are in very close agreement, which is expected in this low frequency regime away from the first cutoff frequency.

IDT wave mode selection capability is illustrated in Fig. 6 for a 1.25MHz, 10 cycles input signal, which is used to independently excite modes a_0, s_0 and a_1 in a 2mm thick aluminium plate. From Fig. 3a, the finger spacing of the corresponding IDT are determined to be 1.11mm, 1.59mm and 2.80mm, respectively. To reduce the wave number bandwidth the widths of the IDT fingers are apodised using a Hanning window modulation similar to the sinusoidal excitation pulse. Thus, the widths of the individual fingers are

$$a_k = \frac{a_c}{2}\left[1-\cos(\frac{2k}{n_f}\pi)\right], \quad k=1, 2, \ldots n_f \tag{27}$$

where a_c is the width of the central finger. Fig. 6 shows the surface velocity time histories at a distance of 300mm from the IDT. The arrival times of the wave groups confirm that the three response signals correspond to the three target modes of the individual IDT.

As a comparison, Fig. 7 shows the surface velocity response at the same measurement location excited by a conventional bulk transmitter element, which can be considered as a transducer formed by combining all the fingers of the IDT. The comparison with the individual wave mode response signals displayed in Fig. 6 shows that the first wave group in Fig. 7 is mainly due to the contribution from mode a_1, and the second is due to the contribution from mode s_0. It is also important to realise that the amplitude of the surface velocity signal for the bulk transmitter is approximately 40 times smaller than the signals generated by the IDT. The input wave number spectrum defined by (16) provides a means to explain these results. Fig. 8 shows the input wave number spectra for the three IDT and the bulk transmitter element. The centre wave numbers of the IDT are located at the positions corresponding to the wave number-frequency graph displayed in Fig. 3a. Thus, pure wave mode excitation is achieved as expected. However, the input wave number spectrum of the bulk transducer covers the wave number regimes of all wave modes, which may exist at the specific excitation frequency. Hence, several wave modes are excited. In addition, Fig. 8 clearly shows why the amplitudes of the wave groups excited by the bulk transducer are smaller than the single mode pulses excited by the three IDT and why the pulse corresponding to the a_0 mode is barely present in Fig. 7. For a given excitation signal, the amplitude of the input wave number spectrum of the bulk transducer at the wave number regimes of the three wave modes are much smaller

than those of the three mode specific IDT. It turns out that the bulk transducer wave number spectrum is zero very close to the centre wave number of the a_0 mode, which explains why this mode is hardly present in Fig. 7.

There are several factors influencing the output of an IDT. For example, increasing the number of fingers and different apodisation of the finger widths are system parameters with the potential for improving the mode selection capability of an IDT. The following paragraphs examine the influence of wave mode excitability, finger widths distribution, number of fingers and excitation signal features on the output of IDT using the multiple integral transform methodology.

Fig. 9a shows the surface velocity response on a (0°/90°/0°/90°/0°) graphite-epoxy laminate excited by an a_1 target wave mode IDT at 880kHz. Unlike expected, two wave groups are present, the first one related to the a_1 mode and the second to the a_0 mode. Furthermore, the a_1 mode pulse is much smaller than the non-target a_0 mode. The input wave number spectrum in Fig. 9b for the IDT under consideration helps to explain this behaviour. Obviously, there exist several wave number regimes of good wave mode excitability. It turns out that the third regime at around 2800m^{-1} closely matches the wave number regime required for a_0 wave mode excitation.

The reason why the transverse velocity amplitude of the a_0 mode pulse is bigger than the one of the a_1 mode depends on the relative excitability of the out-of-plane velocity component of the eigenmode within the excited frequency regime, which can be determined using (18). It turns out that the excitability of the a_0 mode is approximately 52 times larger than for the a_1 mode. This explains why the a_0 amplitude is considerably larger even if the amplitude in the wave number spectrum is slightly smaller than for the a_1 mode.

In order to enlarge the a_1 mode in Fig. 9a, a possible way is to increase the width of the IDT fingers. Figs. 10 show the changes of the time history and input wave number spectrum if the width of the central finger of the IDT is increased from $2a_c$=1mm to $2a_c$=5.46mm. The wave number spectrum in Fig. 10b shows that the amplitude of the

first high amplitude regime, which corresponds to a_1 mode, is approximately 5 times bigger in amplitude compared to Fig. 9b, while the second one corresponding to the a_0 mode only increases slightly. Hence, it can be expected that the a_1 mode will have an apparent increase in the time trace, while the amplitude of the a_0 mode will remain nearly unchanged. This is exactly what the calculated time trace result in Fig. 10a shows. This demonstrates that proportionally increasing the widths of the IDT fingers provides a way to modify the IDT's output, in addition to the commonly used methods of increasing the number of fingers and changing the finger apodisation.

In Fig. 11, the influence of the overall width of the IDT on its output is examined. Referring to the case considered in Figs. 10, the overall width of the IDT is increased by changing the number of fingers from 20 to 30, and keeping finger spacing and shape of the apodisation window identical. The increase of the overall IDT width results in a major change in the a_0 pulse shape. The previous single group obviously separates into two groups. The reason is that the wave propagation is sufficiently non-dispersive that the wave pulse issued from the front or right edge of the IDT is leading the pulse simultaneously excited from the back or left edge of the transducer. The start and end time t_1 and t_2 of the a_0 mode indicated in Fig. 11 are calculated as

$$t_1 = \frac{x_0 - (n_f - 1)d - a_{n_f}}{c_g}, \qquad t_2 = \frac{x_0 + a_1}{c_g} + T \tag{28a,b}$$

where, referring to Fig. 2, x_0 is the distance of the observation point away from the origin, d and n_f are the IDT finger spacing distance and the number of fingers, a_1 and a_{n_f} are the half widths of the two fingers at the back and front edge of the IDT, c_g is the group velocity at the central frequency, and T is the duration period of the excitation signal. It turns out that the above formulae provide a helpful tool to estimate the expected arrival time and duration of a wave pulse at a measurement location and hence help choosing an excitation pulse and IDT width, which avoid extensive pulse separation.

It has been shown in Fig. 5 that the simulation results based on Mindlin plate and discrete layer theory are in very close agreement at a frequency well below the cutoff frequency. But it is still of interest to know how well the Mindlin plate theory works at relatively high frequencies considering its potential as a time efficient IDT design tool.

Figs. 12 compare the simulation results based on Mindlin plate and discrete layer theory for the case previously discussed in Figs. 10. Fig. 12a shows that for the a_0 mode the result based on the Mindlin plate theory depicts the major features of the IDT output, although a small time shift of 20μs is observed. However, the comparison of the corresponding a_1 mode results in Fig. 12b shows that the Mindlin plate theory gives a much larger pulse amplitude and pulse duration than the discrete layer theory, although the initial pulse arrival times correspond well. These results illustrate that the Mindlin plate theory can generally not be used for the design of a_1 target mode IDT.

6 CONCLUSIONS

The investigations of the acoustic waves generated in an orthotropic plate by an interdigital transducer have shown that:

1. the analytical-numerical, discrete layer multiple integral transform method provides an effective way to interpret output signal features, especially by considering the transducer's input wave number spectrum beyond the commonly used input frequency spectrum.
2. IDT enable mode selection and isolation, but a large number of parameters, such as finger number, apodisation and widths have to be considered and the availability of an accurate simulation tool is essential for the design of optimised transducers and to avoid unexpected wave modes, especially in the case of non-isotropic materials.
3. some simple equations enable the estimation of the expected start and end arrival times of individual wave groups.
4. it is acceptable to use Mindlin plate theory to design an a_0 target mode IDT, but it cannot be used to design a_1 target mode IDT.

ACKNOWLEDGEMENT

The support for this work by the Australian Research Council under grant A10027167 and the City University of Hong Kong through research grant DAG 7100162 is greatly acknowledged.

APPENDIX

A1 Matrices used in Equation (1)

$$\mathbf{M}^{(i)} = \frac{1}{30} h_i \rho_i \begin{bmatrix} 4\mathbf{I} & 2\mathbf{I} & -\mathbf{I} \\ & 16\mathbf{I} & 2\mathbf{I} \\ \mathbf{Sym.} & & 4\mathbf{I} \end{bmatrix}, \quad \mathbf{K}_1^{(i)} = \frac{1}{30} h_i \begin{bmatrix} 4\mathbf{A}_1 & 2\mathbf{A}_1 & -\mathbf{A}_1 \\ & 16\mathbf{A}_1 & 2\mathbf{A}_1 \\ \mathbf{Sym.} & & 4\mathbf{A}_1 \end{bmatrix},$$

$$\mathbf{K}_4^{(i)} = \frac{1}{6} \begin{bmatrix} -6\mathbf{B}_4 + 3\mathbf{A}_4 & -4\mathbf{A}_4 & \mathbf{A}_4 \\ & 0 & -4\mathbf{A}_4 \\ \mathbf{Antisym.} & & 6\mathbf{B}_4 - 3\mathbf{A}_4 \end{bmatrix},$$

$$\mathbf{K}_6^{(i)} = \frac{1}{3h_i} \begin{bmatrix} 7\mathbf{B}_6 & -8\mathbf{B}_6 & \mathbf{B}_6 \\ & 16\mathbf{B}_6 & -8\mathbf{B}_6 \\ \mathbf{Sym.} & & 7\mathbf{B}_6 \end{bmatrix}$$

in which $\mathbf{I}$ is a 2×2 identity matrix, and $\mathbf{A}_1$, $\mathbf{A}_4$, $\mathbf{B}_4$ and $\mathbf{B}_6$ are given by

$$\mathbf{A}_1 = \begin{bmatrix} c_{11} & c_{15} \\ c_{15} & c_{55} \end{bmatrix}, \qquad \mathbf{A}_4 = \begin{bmatrix} 2c_{15} & c_{13} + c_{55} \\ c_{13} + c_{55} & 2c_{35} \end{bmatrix},$$

$$\mathbf{B}_4 = \begin{bmatrix} c_{15} & c_{55} \\ c_{13} & c_{35} \end{bmatrix}, \qquad \mathbf{B}_6 = \begin{bmatrix} c_{55} & c_{35} \\ c_{35} & c_{33} \end{bmatrix}$$

where c_{ij} (i,j=1,3,5) are the components of the general stiffness matrix for the ith layer

A2 Coefficients used in Equations (24) and (25)

$$\mu_1 = -\frac{1}{D_{11}\omega^2\delta\eta}, \qquad \mu_2 = -\frac{c_0^2\alpha^2\eta}{4D_{11}\omega^2\delta}$$

$$\mu_{11} = \frac{3(i\kappa_1 a_k - 1)}{D_{11}a_k^2\omega\eta\kappa_1^2}, \quad \mu_{11} = \frac{3(i\kappa_1 a_k + 1)}{D_{11}a_k^2\omega\eta\kappa_1^2}$$

$$\mu_{21} = \frac{3c_0^2\alpha^2\eta(i\hat{\kappa}a_k - 1)}{4D_{11}a_k^2\omega^2\delta\hat{\kappa}^2}, \qquad \mu_{22} = \frac{3c_0^2\alpha^2\eta(i\hat{\kappa}a_k + 1)}{4D_{11}a_k^2\omega^2\delta\hat{\kappa}^2}$$

$$\kappa_1 = \left[\frac{1}{2}\left(\frac{1}{c_0^2} + \frac{1}{c_s^2}\right)\omega^2 + \sqrt{\frac{1}{4}\left(\frac{1}{c_0^2} - \frac{1}{c_s^2}\right)^2 \omega^4 + \frac{1}{c_0^2\alpha^2}\omega^2} \right]^{1/2}, \qquad \text{for } |\omega| < \infty$$

$$\gamma = \left[\sqrt{\frac{1}{4}\left(\frac{1}{c_0^2} - \frac{1}{c_s^2}\right)^2 \omega^4 + \frac{1}{c_0^2 \alpha^2}\omega^2} - \frac{1}{2}\left(\frac{1}{c_0^2} + \frac{1}{c_s^2}\right)\omega^2 \right]^{1/2}, \qquad \text{for } |\omega| \le \omega_c$$

$$\kappa_2 = \left[\frac{1}{2}\left(\frac{1}{c_0^2} + \frac{1}{c_s^2}\right)\omega^2 - \sqrt{\frac{1}{4}\left(\frac{1}{c_0^2} - \frac{1}{c_s^2}\right)^2 \omega^4 + \frac{1}{c_0^2 \alpha^2}\omega^2} \right]^{1/2}, \qquad \text{for } |\omega| > \omega_c$$

in which

$\hat{\kappa} = -i\gamma$ for $|\omega| \le \omega_c$

$\hat{\kappa} = \kappa_2$ for $|\omega| > \omega_c$.

$$\eta = \delta + (1/c_0^2 - 1/c_s^2)\omega, \quad \delta = \left[\left(\frac{1}{c_0^2} - \frac{1}{c_s^2}\right)^2 + \frac{4}{c_0^2 \alpha^2} \right]^{\frac{1}{2}}$$

$$c_0 = \sqrt{\frac{12 D_{11}}{\rho h^3}}, \quad c_s = \sqrt{\frac{A_{55} k_s}{\rho h}}, \quad \alpha = \frac{h}{\sqrt{12}}$$

REFERENCES

[1] J.L. Rose, Recent advances in guided wave NDE, IEEE Ultrasonics Symposium, 1995, pp.761-770.

[2] P. Wilcox, M. Castaings, R. Monkhouse, P. Cawley, and M. Love, An example of the use of interdigital PVDF transducers to generate and receive a high order Lamb wave mode in a pipe, Review of Progress in Quantitative Nondestructive Evaluation, Vol.16, 1997, pp.919-926.

[3] R.S.C. Monkhouse, P.D. Wilcox and P. Cawley, Flexible interdigital PVDF Lamb wave transducers for the development of smart structures, Review of Progress in Quantitative Nondestructive Evaluation, Vol.16, 1997, pp.877-884.

[4] A. Gachagan, G. Hayward, A. McNab, P. Reynolds, S.G. Pierce, W.R. Philp and B. Culshaw, Generaction and reception of ultrasonic guided waves in composite plates using conformable piezoelectric transducers and optical-fiber detectors, IEEE Transactions on Ultrasonics, Ferroelectrics, and Frequency Control, Vol. 46, 1999, pp.72-81.

[5] P. Wilcox, R. Monkhouse, M. Love and P. Cawley, The use of "Huygens" Principle to model the acoustic field from interdigital Lamb wave transducers, Review of Progress in Quantitative Nondestructive Evaluation, Vol.17, 1998, pp.915-922.

[6] S.B. Dong and R.B. Nelson, On natural vibrations and waves in laminated orthotropic plates, Journal of Applied Mechanics, Vol. 39, 1972, pp.739-745.

[7] S.B. Dong and K.H. Huang, Edge vibrations in laminated composite plates, Journal of Applied Mechanics, Vol. 52, 1985, pp.433-438.

[8] K. Kausel, Wave propagation in anisotropic layered media, International Journal of Numerical Methods in Engineering, Vol. 23, 1986, pp.1567-1578.

[9] G.R. Liu, J. Tani, T. Ohyoshi and K. Watanabe, Transient waves in anisotropic laminated plates. part I: theory, Journal of Vibration and Acoustics, Vol. 113, pp. 230-234.

[10] C.T. Sun and R.Y.S. Lai, Exact and approximate analysis of transient wave propagation in an anisotropic plate, AIAA Journal, Vol. 12, 1974.

[11] P.D. Wilcox, P. Cawley and M.J.S. Lowe, Acoustic fields from PVDF interdigital transducers, IEE Proc. Csi. Meas. Technol., Vol. 145, 1998, pp.250-259.

FIGURE CAPTIONS

Fig. 1: An interdigital transducer attached to an orthotropic plate to excite single Lamb wave modes.

Fig. 2: Sketch of major system parameters.

Fig. 3: a) Wavenumber vs. frequency and b) group velocity vs frequency curves for a 2mm thick aluminum plate.

Fig. 4: a) Wavenumber vs. frequency and b) group velocity vs frequency curves for a 2mm thick, (0°/90°/0°/90°/0°) graphite-epoxy plate.

Fig. 5: Surface velocity time history; Al plate h=2mm; measurement location x_0=300mm; IDT n_f=20, a=0.5mm, d=3.768mm, target mode a_0; excitation f_0=250kHz; solid line: discrete layer theory; dashed line: Mindlin plate theory.

Fig. 6: Surface velocity time histories; Al plate h=2mm; measurement location x_0=300mm; IDT n_f=20, apodised fingers a_c=0.5mm; excitation f_0=1.25MHz, a) target mode a_0, d=λ/2=1.11mm; b) target mode s_0, d=λ/2=1.59mm; c) target mode a_1, d=λ/2=2.80mm.

Fig. 7: Surface velocity time histories; Al plate h=2mm; measurement location x_0=300mm; bulk transmitter; excitation f_0=1.25MHz.

Fig. 8: Input wave number spectra; bulk transducer; IDT-1 target mode a_0, d=λ/2=1.11mm; IDT-2 target mode s_0, d=λ/2=1.59mm; IDT-3 target mode a_1, d=λ/2=2.80mm.

Fig. 9: a) Surface velocity time history; (0°/90°/0°/90°/0°) G-E laminate, h=2mm; measurement location x_0=300mm; IDT n_f=20, apodised fingers a_c=0.5mm, target mode a_1, d=λ/2=5.47mm; excitation f_0=880kHz; b) corresponding wave number spectrum.

Fig. 10: a) Surface velocity time history; (0°/90°/0°/90°/0°) G-E laminate, h=2mm; measurement location x_0=300mm; IDT n_f=20, apodised fingers a_c=2.7mm, target mode a_1, d=λ/2=5.47mm; excitation f_0=880kHz; b) corresponding wave number spectrum.

Fig. 12: Surface velocity time histories for discrete layer theory (solid line), Mindlin plate theory (dashed line); (0°/90°/0°/90°/0°) G-E laminate, h=2mm; measurement location x_0=300mm; IDT n_f=20, apodised fingers a_c=2.7mm, target mode a_1, d=λ/2=5.47mm; excitation f_0=880kHz; a) a_0 wave mode pulse b) a_1 wave mode pulse.

Table 1: Properties of aluminium (Al) and graphite-epoxy (G-E) lamina

Material	E_1 [GPa]	E_2 [GPa]	G_{12} [GPa]	G_{13} [GPa]	G_{23} [GPa]	ν_{12}	ρ [kg/m^3]
Al	73	73	28.077	28.077	28.077	0.3	2770
G-E	137.9	8.957	7.102	7.102	6.206	0.3	1578

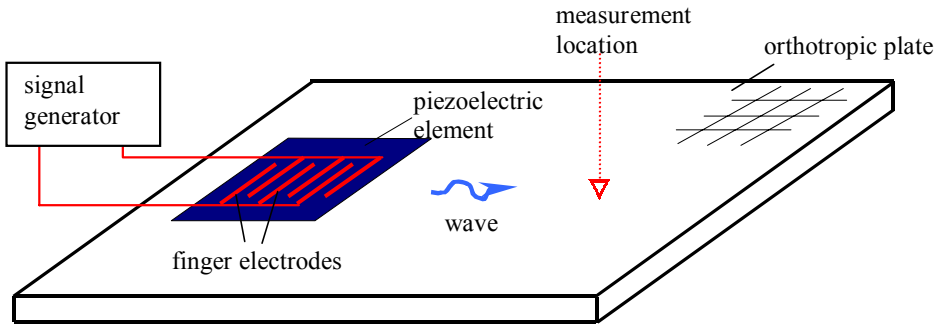

Fig. 1: An interdigital transducer attached to an orthotropic plate to excite single Lamb wave modes.

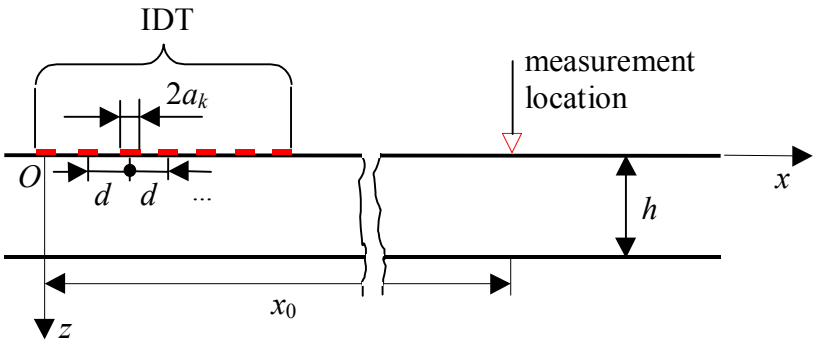

Fig. 2: Sketch of major system parameters.

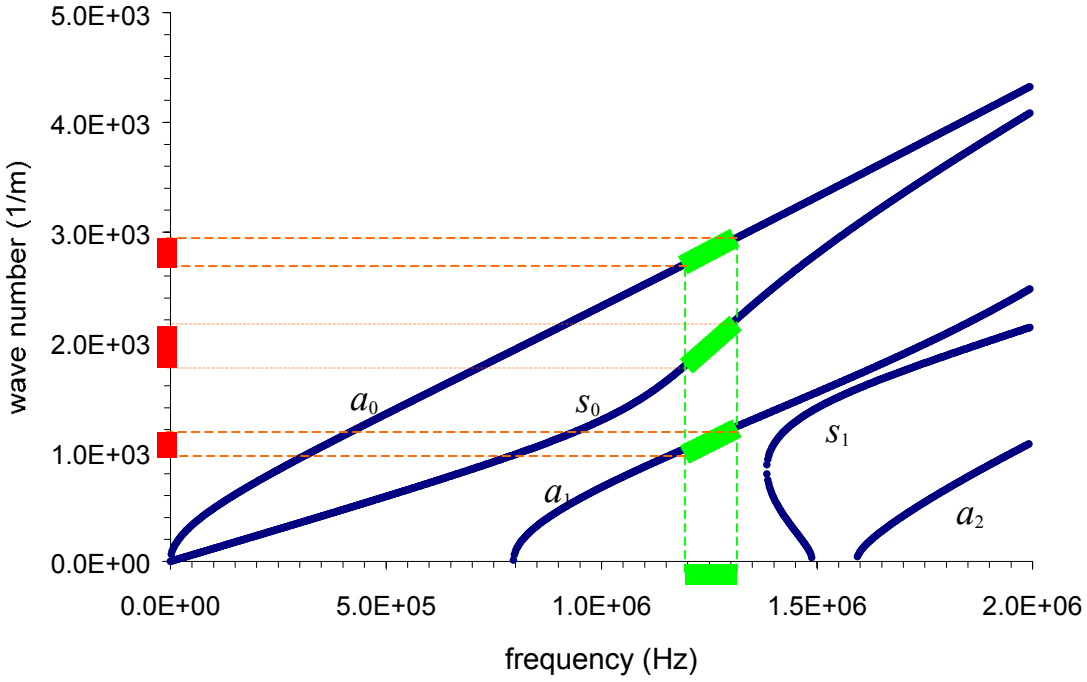

a)

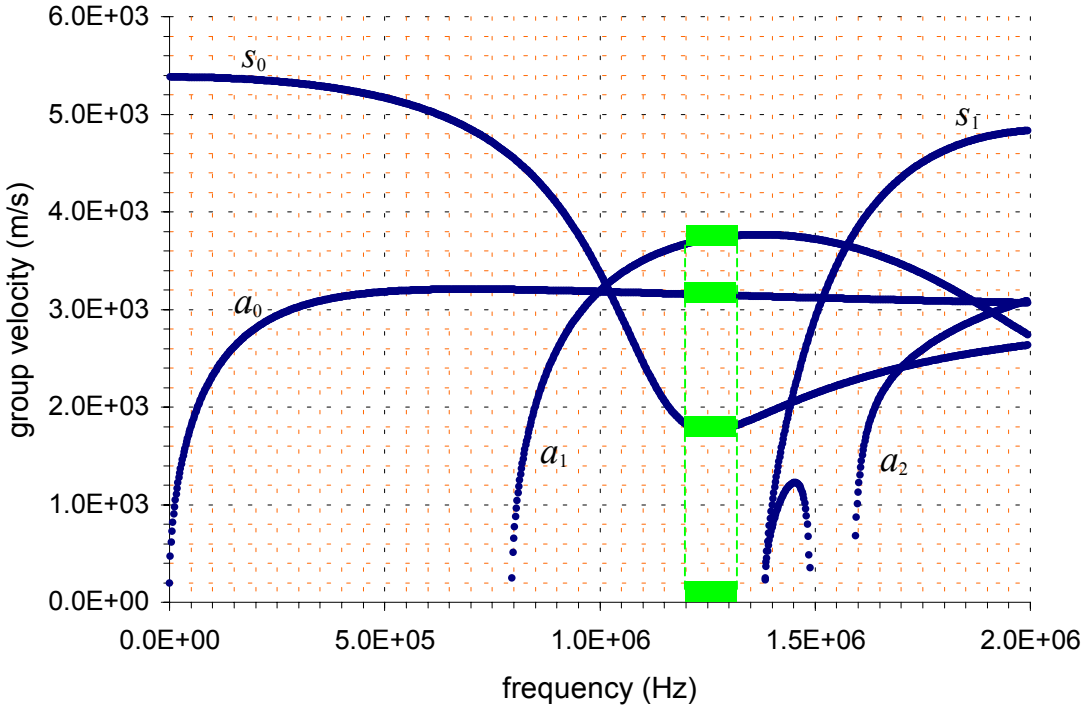

b)

Fig. 3: a) Wavenumber vs. frequency and b) group velocity vs frequency curves for a 2mm thick aluminum plate.

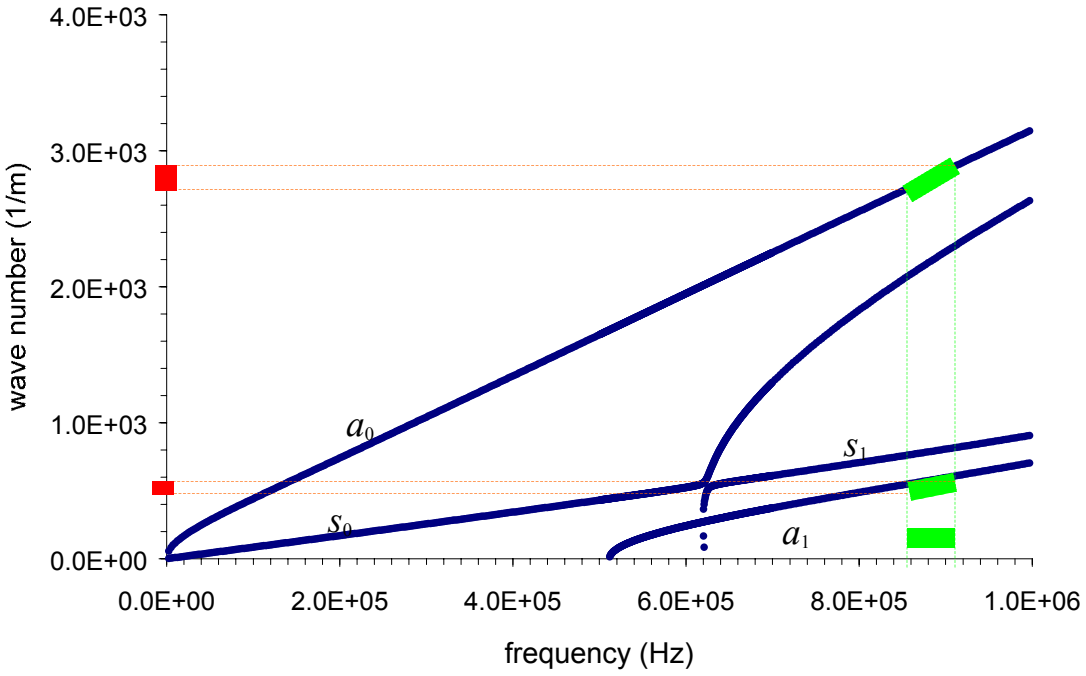

a)

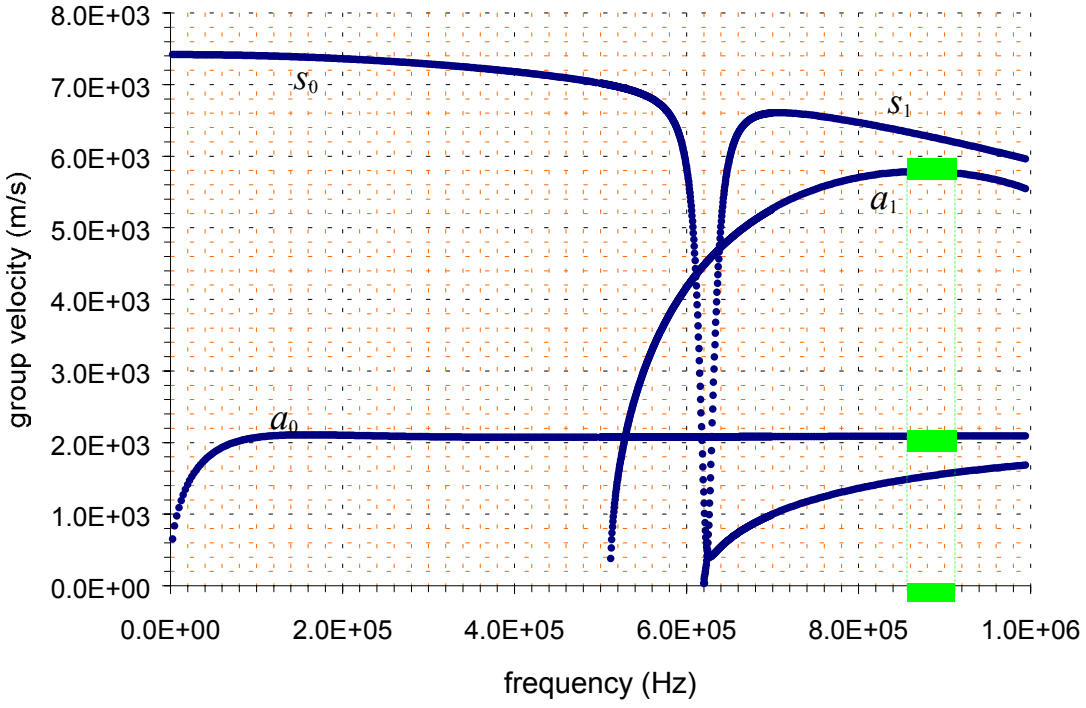

b)

Fig. 4: a) Wavenumber vs. frequency and b) group velocity vs frequency curves for a 2mm thick, (0°/90°/0°/90°/0°) graphite-epoxy plate.

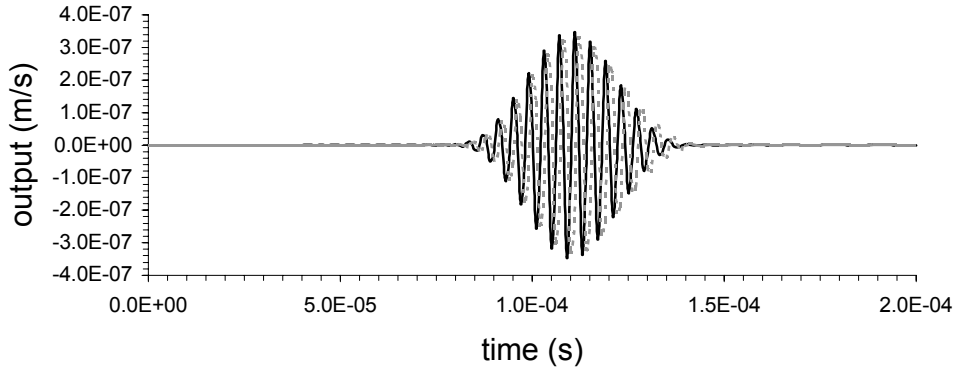

Fig. 5: Surface velocity time history; Al plate h=2mm; measurement location x_0=300mm; IDT n_f=20, a=0.5mm, d=3.768mm, target mode a_0; excitation f_0=250kHz; solid line: discrete layer theory; dashed line: Mindlin plate theory.

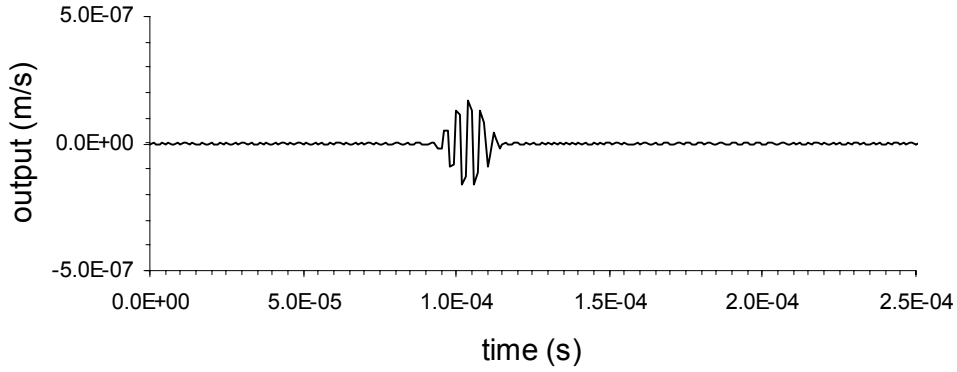

a)

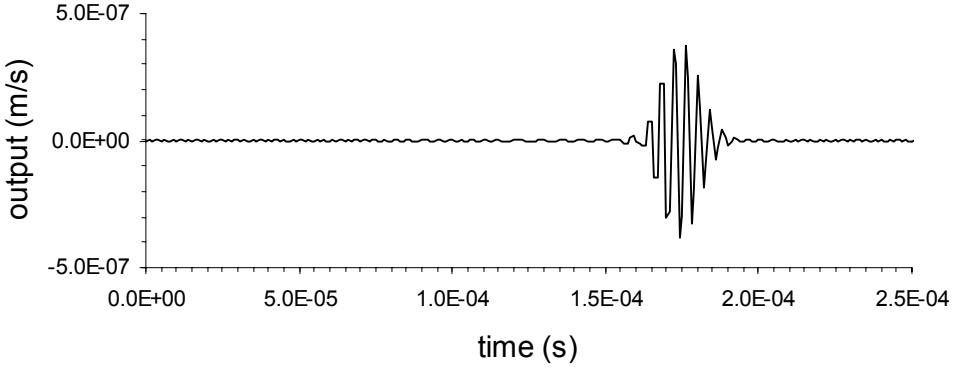

b)

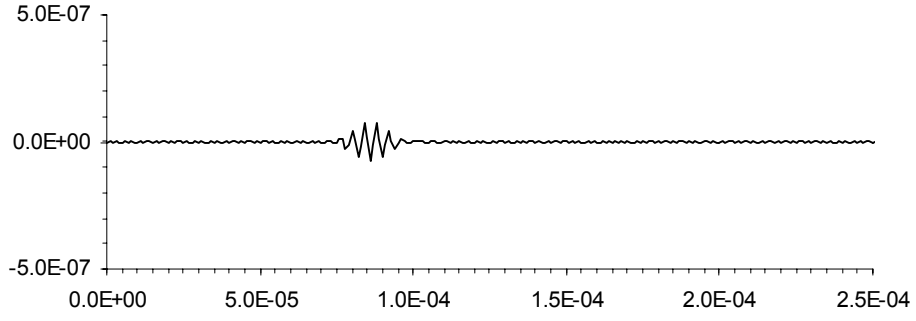

c)

Fig. 6: Surface velocity time histories; Al plate h=2mm; measurement location x_0=300mm; IDT n_f=20, apodised fingers a_c=0.5mm; excitation f_0=1.25MHz, a) target mode a_0, d=λ/2=1.11mm; b) target mode s_0, d=λ/2=1.59mm; c) target mode a_1, d=λ/2=2.80mm.

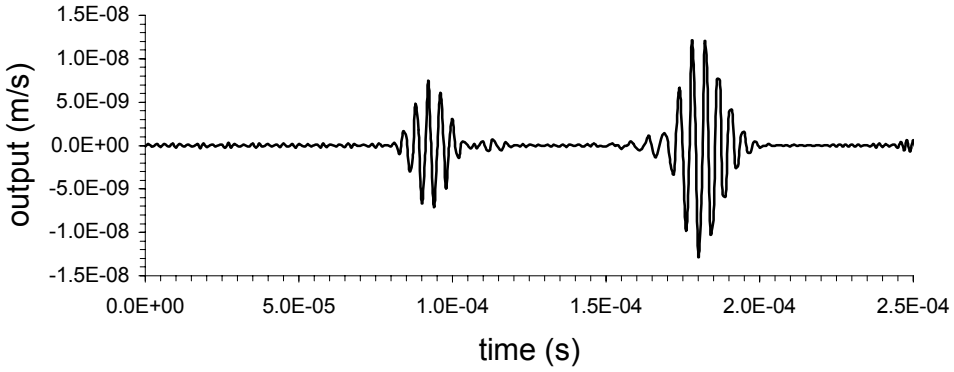

Fig. 7: Surface velocity time histories; Al plate h=2mm; measurement location x_0=300mm; bulk transmitter; excitation f_0=1.25MHz.

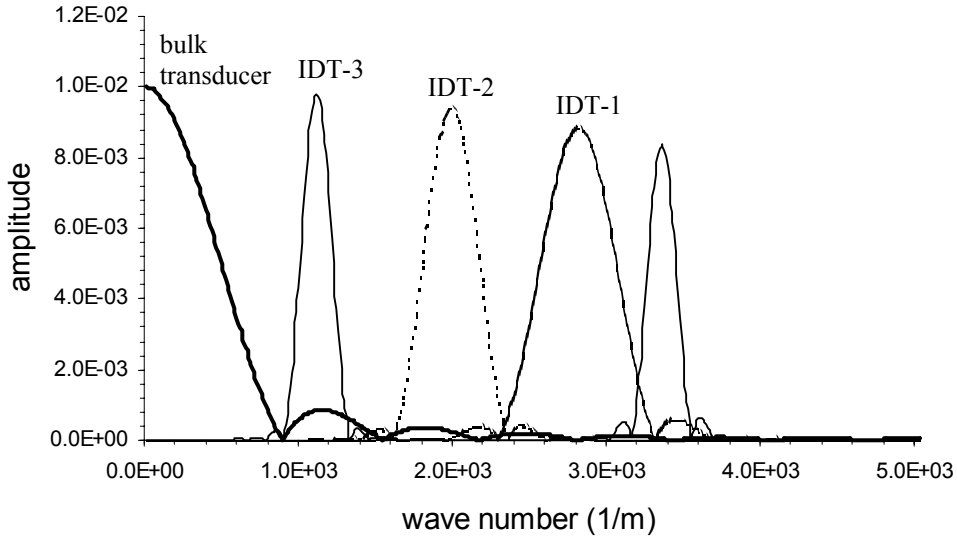

Fig. 8: Input wave number spectra; bulk transducer; IDT-1 target mode a_0, d=λ/2=1.11mm; IDT-2 target mode s_0, d=λ/2=1.59mm; IDT-3 target mode a_1, d=λ/2=2.80mm.

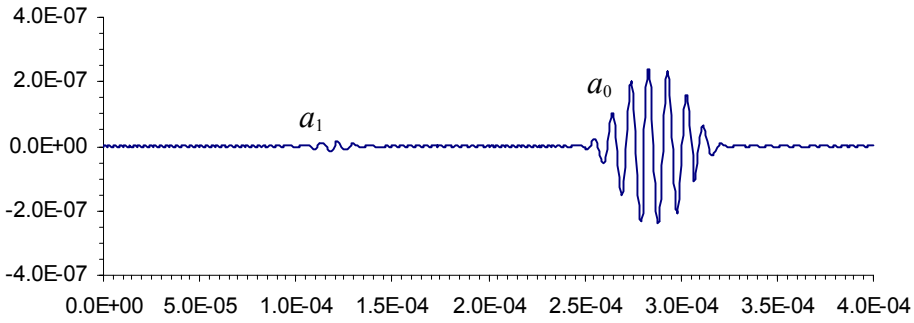

a)

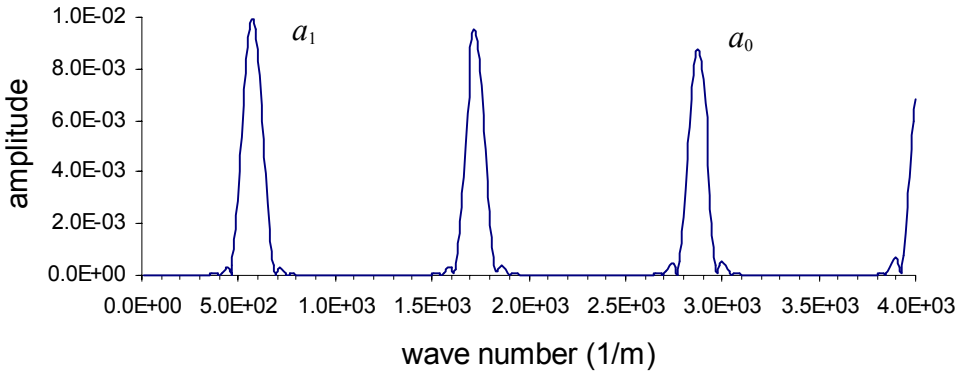

b)

Fig. 9: a) Surface velocity time history; (0°/90°/0°/90°/0°) G-E laminate, h=2mm; measurement location x_0=300mm; IDT n_f=20, apodised fingers a_c=0.5mm, target mode a_1, d=λ/2=5.47mm; excitation f_0=880kHz; b) corresponding wave number spectrum.

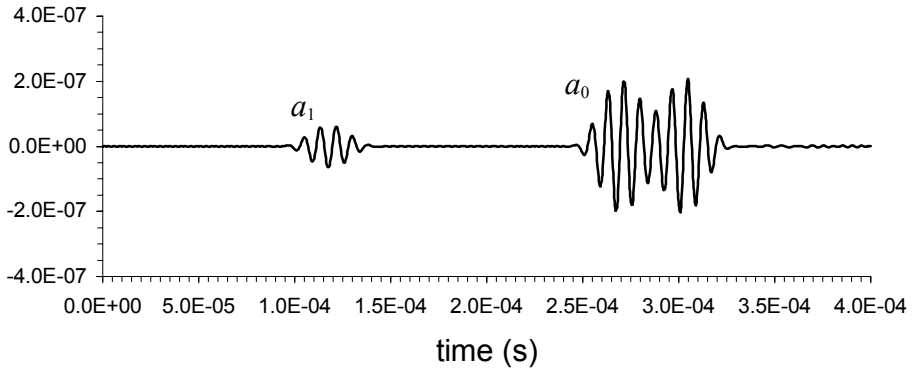

a)

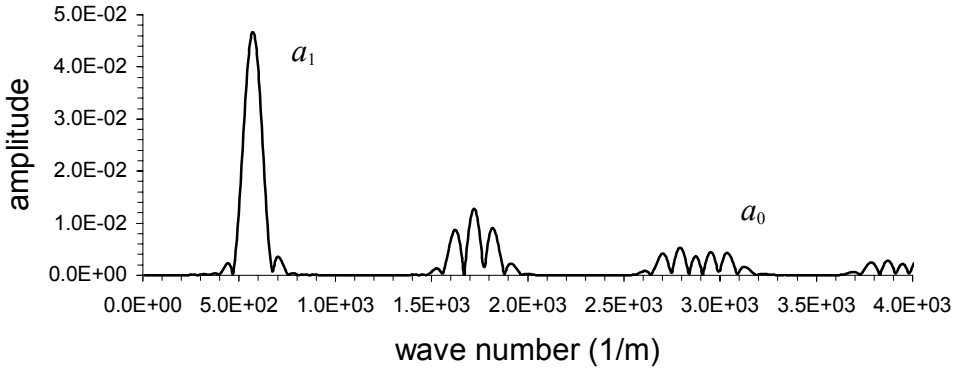

b)

Fig. 10: a) Surface velocity time history; (0°/90°/0°/90°/0°) G-E laminate, h=2mm; measurement location x_0=300mm; IDT n_f=20, apodised fingers a_c=2.7mm, target mode a_1, d=λ/2=5.47mm; excitation f_0=880kHz; b) corresponding wave number spectrum.

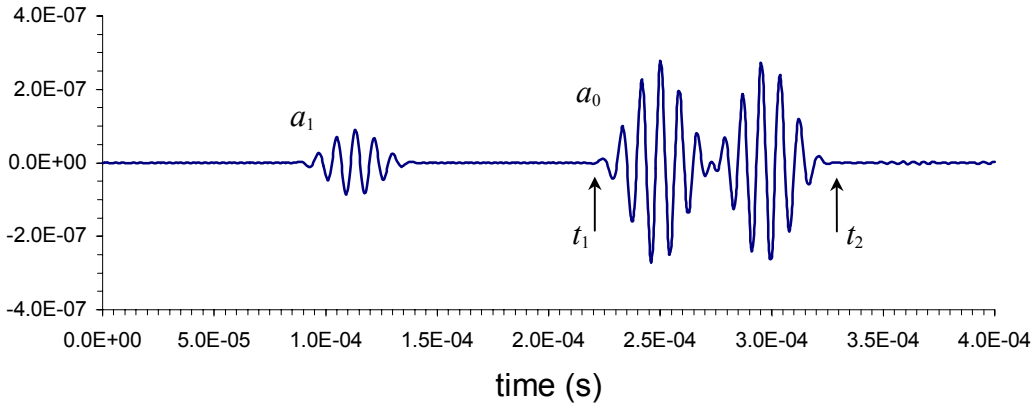

Fig. 11: Surface velocity time history; (0°/90°/0°/90°/0°) G-E laminate, h=2mm; measurement location x_0=300mm; IDT n_f=30, apodised fingers a_c=2.7mm, target mode a_1, d=λ/2=5.47mm; excitation f_0=880kHz.

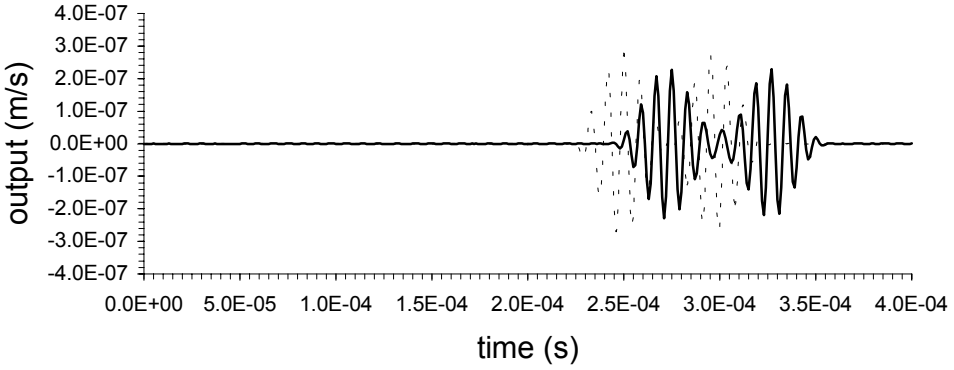

a)

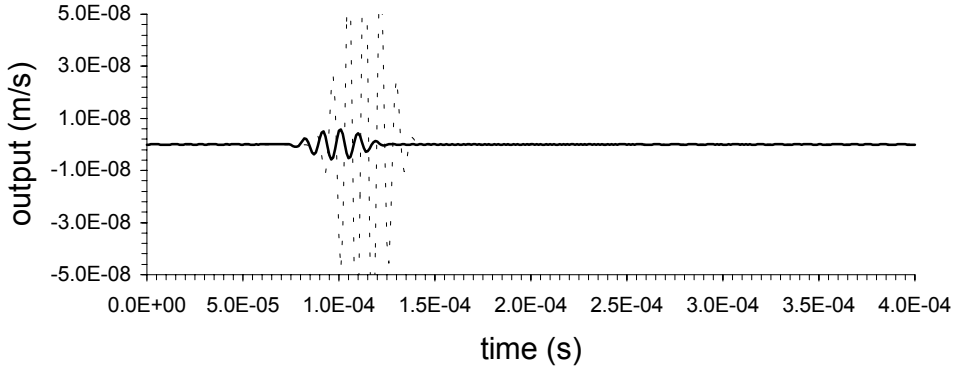

b)

Fig. 12: Surface velocity time histories for discrete layer theory (solid line), Mindlin plate theory (dashed line); (0°/90°/0°/90°/0°) G-E laminate, h=2mm; measurement location x_0=300mm; IDT n_f=20, apodised fingers a_c=2.7mm, target mode a_1, d=λ/2=5.47mm; excitation f_0=880kHz; a) a_0 wave mode pulse b) a_1 wave mode pulse.